New perspectives on 'geological strain rates' calculated from both naturally deformed and actively deforming rocks

Åke Fagereng[a], Juliet Biggs[b]

[a]*School of Earth & Ocean Sciences, Cardiff University, United Kingdom*
[b]*School of Earth Science, University of Bristol, United Kingdom*

Abstract

A value of $\sim 10^{-14}$ s^{-1} is commonly cited as an average geological strain rate. This value was first suggested for finite strain across an orogen, but based on more limited information than the combined geophysical, geological, and experimental data now available on active and ancient rock deformation. Thus, it is timely to review the data constraining strain rates in the continents, and to consider the quantifiable range of crustal strain rates. Here, where resolution allows, both spatial and temporal strain rate variations are explored. This review supports that a strain rate of $10^{-14\pm1}$ s^{-1} arises from geological estimates of bulk finite strains. Microstructural arguments combining laboratory-derived piezometers and viscous flow laws, however, imply local rates that are orders of magnitude faster. Geodetic rates, in contrast, are typically $\sim 10^{-15}$ s^{-1} in actively deforming areas, about an order of magnitude slower than the bulk rates estimated from geological observations. This difference in estimated strain rates may arise from either low spatial resolution, or the fact that surface velocity fields can not capture strain localisation in the mid to lower crust. Integration of geological and geodetic

rates also shows that strain rates can vary in both space and time, over both single and multiple earthquake cycles. Overall, time-averaged geological strain rates are likely slower than the strain rates in faults and shear zones that traverse the crust or lithosphere.

Keywords: strain rate, rock deformation, geodesy, faults, shear zones

1. Introduction

Pfiffner and Ramsay (1982) suggested a 'conventional geological strain rate' of $10^{-14\pm1}$ s^{-1}. This estimate has been widely applied since the publication of their now classic paper, which was based on the finite strain record of orogenic belts. However, Pfiffner and Ramsay (1982) begin their article by stating that data on rates of natural rock deformation are rare. At the time of their writing, geodetic surveys of the San Andreas fault (Whitten, 1956) and measurements of glacial isostatic adjustment (Hicks and Shofnos, 1965) were the main sources of such data. Today, modern geodesy has hugely increased the data set on directly measured surface deformation. In addition, decades of rock deformation experiments and microstructural studies have led to new inferences regarding the mechanisms and rates of rock deformation based on the rock record. Collection and analysis of seismological data have also greatly increased knowledge of how this deformation is distributed in space and time. Huntington et al. (2018) raise the understanding of rheological variations through the lithosphere, for which strain rate distribution is a critical constraint, as a current Grand Challenge in tectonics research. This is therefore an appropriate time to revisit the outcrop record of rock deformation in light of new geodetic, seismic, and laboratory data, and to

discuss the calculation and interpretation of a 'geological strain rate'. In particular, we consider the following three questions:

1. What is the observed, quantifiable, range of strain rates in nature?
2. How does strain rate vary in space, and to what degree is strain localised onto crustal-scale fault zones?
3. How does strain rate vary in time, not only through individual earthquake cycles, but also across geological timescales?

We consider these questions from two distinct perspectives: first we discuss continental strain over lengthscales greater than the lithospheric thickness and timescales of multiple earthquake cycles. We then consider how variations in strain with depth during different phases of the earthquake cycle (a) translate into surface strain and (b) are recorded within fault zone rocks.

2. Definitions of Strain Rate

Strain, and its derivative, strain rate, are formally described by a second order tensor, but for the purposes of discussion, we primarily use the scalar magnitude, which can be defined in a variety of ways. Longitudinal strain, e, is the change in length of a linear element, Δl, divided by its original length prior to a discrete deformation episode, l_0. Alternatively, one may calculate natural strain, ϵ, where strain is defined as having occurred over multiple infinitesimal increments, each deforming a linear element that includes all the previous deformation increments, i.e. $\epsilon = \int_{l_0}^{l_f} \frac{dl}{l}$, where l_f is the final length.

Shear strain rate in simple shear can be considered in terms of shear strain accumulated within an idealised shear zone of width, w, accommodating a finite displacement, d, parallel to its boundaries. In this case, shear strain is defined as $\gamma = d/w$ and the shear strain rate is $\dot{\gamma} = \gamma/t = s/w$ where s is the velocity difference across the shear zone. In simple shear, shear strain rate is therefore critically dependent on the deforming shear zone thickness (Fig. 1a).

To express three dimensional strain, one can define principal strains as the longitudinal strains perpendicular to planes of zero shear strain. The strain ellipsoid represents strain relative to an originally undeformed sphere, and is defined by the principal strains $X \geq Y \geq Z$, where $X = (1 + e_x)$ and $Z = (1 + e_z)$ represent the greatest and least stretch, respectively. Strain rate ($\dot{e}$), is typically calculated by dividing longitudinal finite strain by the time taken to accumulate it. However, we note that Pfiffner and Ramsay (1982) explored the effect of strain path and found that among end-member strain histories and combinations thereof, pure shear is the most, and simple shear the least efficient at accumulating longitudinal strain after any given time period at a constant $\dot{e}$. Here, we will refer to $\dot{e} = \dot{e_x}$ as the greatest longitudinal strain rate at a given location, comparable with what is typically measured in laboratory experiments, or shear strain rate, $\dot{\gamma}$.

3. Crustal-scale strain over multiple earthquake cycles

3.1. Geological Strain Rates

Pfiffner and Ramsay (1982) arrived on a longitudinal, average, conventional geological strain rate of 10^{-14} s^{-1} by considering calculations of bulk

finite strain across orogens, a range of potential strain paths, and geochronological constraints on the time taken to accumulate such strain. Updated constraints on such bulk strain accumulation rates have been obtained since. For example, in the Lachlan orogen, Australia, Foster and Gray (2007) estimate 67 % bulk shortening based on restored thrust sheets, and determine from $^{40}Ar/^{39}Ar$ dating of white mica that deformation lasted approximately 16 million years. This gives an average strain rate ($\dot{e}$) on the order of 10^{-15} s^{-1} assuming deformation was evenly distributed in space and time. The authors note, however, that deformation could have occurred in much shorter pulses, giving a bulk strain rate as fast as 1×10^{-14} s^{-1}. These rates reflect bulk deformation within a km-scale volume of rock, but result from a combination of localised thrust displacements and distributed folding. The latter represent zones of higher and lower strain, respectively, and thus record slower and faster strain rates embedded within the deformed volume (Fig. 1a).

Another approach to estimating strain rate in exhumed rocks is to infer paleostress from microstructures in viscously deformed rocks, constrain temperature of deformation through a geothermometer, and put resulting values into empirically derived flow laws to calculate strain rate. This methodology has the advantage of allowing spatial variations in strain rate to be explored. To this end, a number of authors have used quartz paleopiezometry to estimate stresses involved in quartz deformation by dislocation creep, based on the empirical relationship (Twiss, 1977):

$$\Delta\sigma = BD^{-p} \tag{1}$$

which relates steady-state differential stress, $\Delta\sigma$, to recrystallised grain size,

D, through the empirical constants p and B that depend on the microscale dynamic recrystallisation mechanism. The steady state shear stress can then be related to the strain rate accommodated by dislocation creep through a flow law

$$\dot{e} = \Delta\sigma^n A \exp\left(-Q/RT\right) \tag{2}$$

where A is a material constant, Q is activation energy, T is temperature in Kelvin, R is the universal gas constant, and n is the stress exponent which depends on the active deformation mechanism. Assuming a constant temperature and steady flow at constant stress, strain rate can therefore be calculated from the recrystallised grain size by calculating flow stress in Eq. 1 and extrapolating a laboratory flow law to this stress in Eq. 2.

This method takes advantage of advances in laboratory rock deformation experiments since the work of Pfiffner and Ramsay (1982), but involves uncertainties in extrapolating flow laws from laboratory to nature, estimating temperature of deformation to calculate strain rate from driving stress, in addition to the inherent error in the laboratory piezometer and flow law calibrations. These uncertainties are difficult to quantify, but could exceed an order of magnitude in the final absolute strain rate estimate (cf. Hacker et al., 1990). To minimise the effect of absolute uncertainty on our conclusions, we will emphasise relative strain rate variations within a region. In the studies we discuss, the authors measured grain size in monominerallic domains to avoid grains whose growth was limited by pinning. However, in multiphase rocks there is additional uncertainty arising because grain size may deviate from the equilibrium state inferred by laboratory piezometer calibrations.

Gueydan et al. (2005) studied spatial variation in strain rate within the exhumed Tinos metamorphic core complex, Greece. They report recrystallised quartz grain size ranging from 160 μm to about 40 μm in distributed and localised ductile deformation zones respectively. Using the quartz piezometer of Stipp and Tullis (2003) and the dislocation creep flow law of Luan and Paterson (1992), these grain sizes imply ductile flow at strain rates of 1.5×10^{-15} s^{-1} and 2.6×10^{-14} s^{-1}, for penetrative and localised ductile flow, respectively (Gueydan et al., 2005). However, scatter in the data implies that within the penetrative ductile flow regime, local strain rate variations are over an order of magnitude faster and slower than the mean inferred strain rate, and within shear zones, strain rate may locally be close to 10^{-13} s^{-1} (Gueydan et al., 2005). Adjacent to the main brittle detachment, ductilely deformed quartz shows a strain rate increase to 2×10^{-12} s^{-1}.

Similarly, strain rates locally elevated to faster than 10^{-14} s^{-1} have been reported from mylonitic gneisses in extended middle crust in the Whipple Mountains, California (Hacker et al., 1992). Behr and Platt (2011), however, suggest that this local increase in strain rate is a result of progressive strain localisation during exhumation along the Whipple Mountain detachment.

Spatial variations in geologically determined strain rates have also been quantified in the Red River and Karakorum shear zones, which are strike-slip zones exhumed from the lower crust. Boutonnet et al. (2013) combined stress estimates from the quartz paleopiezometer of Shimizu (2008) and the laboratory-derived stress-strain rate relationship of Hirth et al. (2001) and calculated strain rates less than 10^{-15} s^{-1} in low strain areas, and greater

than 10^{-13} s^{-1} within localised high strain zones considered to have deformed at the same pressure-temperature conditions. The shear zones considered by Boutonnet et al. (2013) are a few kilometres wide, and represent a 1000-fold increase in shear strain rate relative to the surrounding low strain blocks.

In the exhumed mylonitic hanging wall of the transpressional Alpine Fault, New Zealand, finite shear strains of ≤ 300 were calculated from ductilely deformed pegmatites within a kilometre-wide mylonite-ultramylonite zone (Norris and Cooper, 2003). To our knowledge, these are the largest shear strains directly calculated from rock exposures. The strain distribution across the Alpine fault, as determined from deformed pegmatites, is best explained if lower crustal deformation along the Alpine fault is localised in a 1 - 2 km wide zone (Norris and Cooper, 2003), implying elevated strain rates where strain is localised in the lower crust, here as well as in Tinos, Karakorum and Red River (described above). Uplift on the Alpine fault occurred over the last 5 Ma (Suther, 1995), such that a total, integrated shear strain as high as 300 implies an average shear strain rate of at least 2×10^{-12} s^{-1} in localised zones. Based on paleopiezometry and Ti-in-quartz geothermometry, Cross et al. (2015) determined a strain rate range for Alpine fault zone mylonites deformed at 450-500°C, and preferred a value on the order of 10^{-13} s^{-1}.

The method and examples above rely on the rock record of dislocation creep in quartz. It is, however, likely that other mineral scale deformation mechanisms, such as diffusion creep, also accommodate significant strain rates in the mid- to lower crust. For example, as recrystallisation in high strain zones leads to grain size reduction, a transition from dislocation creep

to a grain-size sensitive flow mechanism can occur (e.g. Platt, 2015). The strain rate in shear zones accommodating flow by grain-size-sensitive creep cannot be directly obtained from a paleopiezometer, as the proportionality between stress and grain size no longer applies. However, for the strike-slip Pernambuco shear zone in Brazil, Viegas et al. (2016) identified deformed quartz ribbons and monominerallic quartz veins within a polyphase ultramylonite dominated by fine-grained feldspar. Based on microstructures and EBSD analyses, the authors infer the dominant deformation mechanism to be diffusion creep in feldspar, and dislocation creep in quartz ribbons. Viegas et al. (2016) therefore determined flow stresses from the quartz veins and ribbons, and through flow laws for dislocation creep in quartz and diffusion creep in feldspar estimated strain rates ranging from 10^{-10} s^{-1} to 10^{-8} s^{-1}. These estimates, if correct, imply at least local and transient increases in shear zone strain rate, accommodated by viscous mechanisms, to 10^{-10} s^{-1} or greater.

We have now listed a number of examples where geological constraints indicate that strain is focused into relatively narrow zones. In most of these examples, the narrow zones are interpreted as established at mid- to lower crustal depths, but note that there are also examples where strain localisation results from progressive deformation during exhumation to lower temperatures and pressures in an extensional tectonic regime (Behr and Platt, 2011). On the crustal scale, localisation of strain into plate boundary zones weakened by grain size reduction, increased temperature, or elevated fluid content, was discussed by Bürgmann and Dresen (2008). These authors suggested the 'banana split' model for lateral strength reduction between stronger conti-

nental interiors; this model is consistent with the above-average strain rates locally recorded within the high strain zones described above.

3.2. Geodetic strain rate estimates

Whereas geological strain rate estimates are typically based on observations of deformation accumulated over millions of years, geodetic techniques, such as GPS and InSAR, measure current and ongoing surface displacements. By considering the lithosphere to deform as a continuum, surface velocity estimates can be used to calculate surface strain (e.g. Haines and Holt, 1993). This approach is valid when considering horizontal lengthscales several times the brittle, elastic thickness of the lithosphere, and also at shorter lengthscales if faults are considered locked. The Global Strain Rate Map (GSRM v2.1), interpolates horizontal velocities from 18,000 GPS sites to calculate the 2nd invariant of the strain rate tensor $\sqrt{\dot{e}_1^2 + \dot{e}_3^2}$ (Kreemer et al., 2014), equivalent to the maximum strain rate reported in the geological estimates previously discussed. The highest strain rates occur on narrow plate boundaries, particularly at fast-spreading ridges where new crust is created, in which estimated strain rates are as high as 1.4×10^{-13} s^{-1}. Figure 1b shows the distribution of strain rates within the nodes defined as deforming in GSRM 2.1, the majority of which lie in the range $5 \times 10^{-17} - 10^{-14}$ s^{-1}. Examining the distribution of strain rates shows that these values are an order of magnitude lower than the earlier geological estimates of $10^{-14\pm1}$ s^{-1} (Pfiffner and Ramsay, 1982), but that the variance is very similar (Fig. 1b).

Roughly 5% of the area defined as deforming in GSRM 2.1 exhibits a strain rate exceeding 10^{-14} s^{-1}. These rates are concentrated in rapidly deforming zones with dense GPS networks such as the San Andreas fault

zone where GSRM reports strain rates exceeding 10^{-14} s^{-1} compared to 10^{-15} s^{-1} or slower in the surrounding areas (Fig. 2a). These higher strain rate zones also correspond to areas of elevated seismic activity, attesting to localisation of deformation (Fig. 2b). However, comparison between the numerous strain models that have been produced for this well studied region demonstrates that the choice of interpolation scheme for GPS-derived models can lead to large near-fault discrepancies (Hearn et al., 2010). The inclusion of higher-resolution InSAR data is therefore critical to defining strain rates close to active structures (Fialko, 2006; Kaneko et al., 2013; Tong et al., 2013; Elliott et al., 2016). In particular, these InSAR data allow identification of structures that may accommodate locally higher strain rates (Elliott et al., 2016).

By approximating the lithosphere as a thin viscous sheet with vertically averaged forces and properties, continental-scale velocity fields can be used to investigate the rheology of the lithosphere (England and McKenzie, 1982). In such models, the horizontal gradients of the deviatoric stress associated with deformation are balanced by gradients of the gravitational potential energy (GPE). The models are capable of reproducing the first order patterns of deformation well, and typically return viscosities of $10^{21} - 10^{22}$ Pas for a viscous fluid with power law exponent $n = 3$, and strain rates up to 10^{-15} s^{-1} (Table 1). The estimated average strain rate values are an order of magnitude lower than those derived by interpolating the velocity field, and averages from geological constraints, as the thin viscous sheet approach likely smooths out concentrations of strain over length-scales less than the thickness of the lithosphere. Some thin viscous sheet studies report large lateral variations in

rheological properties, for example, larger viscosities associated with semi-rigid microplates and lower values in rapidly deforming areas (Flesch et al., 2000, 2001). In other studies, however, such variations result in a negligible reduction in misfit compared to homogeneous models (England and Molnar, 2015; Walters et al., 2017).

Because they vertically average rheological properties, thin viscous sheet models result in lower strain rates than obtained within models with vertical velocity gradients. Another end-member geodynamic model is the channel flow model, in which low viscosity channels accommodate high strain rate deformation driven by a lithostatic pressure gradient (Royden et al., 1997; Beaumont et al., 2001; Godin et al., 2006). This model has been invoked to explain both lack of shortening and presence of orogen-parallel extension within the Tibetan Plateau (Royden et al., 1997), and also a dynamic link between these two observations (Beaumont et al., 2001). Coupled to focused denudation (Beaumont et al., 2001), channel flow may lead to extrusion of mid-crustal rocks between bounding shear zones. Whereas the lower shear zone will be a thrust, the upper shear zone is either normal or reverse depending on the relative velocity of the channel versus its hanging wall (Godin et al., 2006, and references therein). A commonality for channel flow models is a low viscosity (typically $\leq 10^{19}$ Pas, versus $10^{21} - 10^{22}$ Pas typically returned by thin viscous sheet models) invoked based on weakening by partial melting under thickened crust (e.g. Jamieson et al., 2002). This local weakness will lead to higher strain rates than in depth-averaged thin viscous sheet models. For example, if channel thicknesses vary from 3 to 30 km (cf. Godin et al., 2006), and displacement is on the order of a centimeter per year, aver-

age $\dot{\gamma}$ becomes 10^{-14} to 10^{-13} s^{-1} (Fig. 1a). A range of geodynamic models employ strategies between the end member vertical strain rate average of the thin viscous sheet, and the significant vertical variation in strain rate of the channel flow model.

3.3. Seismological strain rate estimates

Whereas geodetic strain rates represent continuous deformation over some time period, seismic strain rates represent time-averaged slip along faults in earthquakes. By Kostrov summation (Kostrov, 1974; Jackson and McKenzie, 1988), a seismic strain rate tensor can be obtained from earthquake moment tensors determined in a seismic volume over a given time period. Comparing geodetic and seismic strain rates allows comparison of aseismic and seismic deformation in a region. If seismic strain rates are low compared to geodetic strain rates, then either some deformation occurs aseismically, or the time of observation is shorter than the recurrence time of major earthquakes.

A comparison of seismic and aseismic strain rates for Iran, where the combined instrumental and historical earthquake catalogues go back over a millennium, has shown a large contrast in deformation style across the country (Masson et al., 2005). In Zagros, southern Iran, $>$ 95% of strain is accommodated aseismically, although intensive microseismic activity is spatially correlated with this deformation. In contrast, northern Iran experiences large earthquakes that account for 30 - 100% of the geodetically determined strain. A reason for the largely aseismic strain accommodation in southern Iran could be that a salt layer decouples an upper, 8 - 10 km thick, aseismically deforming, sedimentary cover from underlying basement rocks, leading to a thin seismogenic thickness (Jackson and McKenzie, 1988). In

northern Iran, few large earthquakes may accommodate the majority of the displacement because deformation occurs in characteristic earthquakes on a few, major strike-slip faults (Masson et al., 2005). Kreemer et al. (2002) have also argued that low seismicity rates, in regions of high geodetic strain rate along major strike-slip faults, can result from faults hosting few but large characteristic earthquakes. Such regions would lack small earthquakes relative to predictions by a Gutenberg-Richter relationship (Wesnousky, 1994).

Although seismic strain rates may differ from geodetic and geological rates, they are particularly informative where other data are not available, such as for regions, depths, and time periods for which reliable geodetic data do not exist. Masson et al. (2005) found that although magnitudes of seismic and aseismic strain rates differ in places, orientations of principal strain axes are comparable. This observation was also made by Ekström and England (1989), who found that seismic strain rates were systematically smaller than expected from relative plate motions, but provided reliable estimates for the orientations of the principal horizontal strains. Therefore, summation of moment tensors may allow velocity fields to be calculated over time periods much longer than the geodetic record. For example, in deforming Asia the strain rate tensor based on instrumental and historical earthquakes show little difference from the velocity field indicated by paleomagnetic rotations in Cretaceous rocks (Holt and Haines, 1993). Furthermore, seismic strain rates can be estimated at depths were geodetic data are not available, and have for example been used to estimate a strain rate magnitude of $\sim 1 \times 10^{-15}$ s^{-1} within slabs subducted to depths in excess of 75 km, implying significant internal deformation in these deeply subducted slabs of oceanic lithosphere

(Bevis, 1988; Holt, 1995).

3.4. Temporal Variations in Strain Rate

Attempts to correlate decadal geodetic and seismic observations with much longer term geological estimates of strain rate have shed light on temporal strain rate variations at timescales of multiple seismic cycles. For example, tectonic reconstructions of the Hikurangi Margin, North Island, New Zealand, show approximately constant rates since 1.5 Ma (Nicol et al., 2007). These near-constant long-term rates are compatible with geodetic strain estimates reflecting deformation in the last 10 - 15 years (Wallace et al., 2004). Thus, Nicol and Wallace (2007) concluded that on a million year timescale, strain rates can be essentially steady for a significant portion of the seismic cycle, with the corollary that GPS largely measures elastic strains that will be converted to permanent, localised deformation along faults in cosesimic earthquake slip. Similar comparisons between decadal and million year strain rate estimates have been made elsewhere, including the Arabia-Eurasia collision zone (Allen et al., 2004), southwest United States (McCaffrey, 2005), and the Andes (Hindle et al., 2002). Like in New Zealand, these areas of well studied, regional crustal deformation show current geodetically determined strain rates within error of the geological strain rates estimated for the last few million years.

In contrast, the Tibetan Plateau has been an area of considerable controversy. Slip rates on major faults agree between geological and geodetic data; however, geomorphological data suggest more rapid motion over timescales of kyrs. Strain rate maps derived from InSAR and GPS demonstrate that at the present day, strain rates are relatively uniform within the Tibetan

Plateau at 10^{-15} s^{-1} (Wang and Wright, 2012; Garthwaite et al., 2013)(Fig. 2c). Major Tibetan faults accumulate strain at rates generally less than 1 cm/yr, resulting in near negligible increases in surface strain rate. Interestingly, broad zones of slightly elevated strain rate are associated with faults that have experienced recent earthquakes (Wang and Wright, 2012; Garthwaite et al., 2013), for example the Kunlun fault (Garthwaite et al., 2013)(Fig. 2c). In addition, Daout et al. (2018) recently used InSAR data to highlight a wide zone of active strike-slip shear along the Jinsha suture, indicating reactivation of a lithospheric weakness that lacks expression of surface faulting. These observations highlight that long-term time-averaged strain rate estimates need to consider temporal variations within the earthquake cycle. Temporal strain rate variation is also seen in the Central Nevada Seismic Belt, where uplift detected by InSAR can be explained by postseismic mantle relaxation lasting several decades after major earthquakes (Gourmelen and Amelung, 2005).

Chatzaras et al. (2015) have provided a model for time-dependent interaction between rheologically distinct mantle and crust. Their model is based on that low resolved shear stresses (less than 10 MPa) are recorded in both the frictional crust and viscous mantle of the San Andreas fault. They suggest an integrated crust-mantle system where distributed mantle deformation controls displacement, and loads the upper crust until its frictional failure strength is reached. This model implies that mantle deformation should accelerate as strain rate increases post-seismically, as seen for example after major earthquakes in southern California (Freed and Bürgmann, 2004), and that the next earthquake will occur where failure strength is first overcome

above a broad deforming zone in the mantle. Although designed for strike-slip faults (Chatzaras et al., 2015), this model may also explain the spatial and temporal strain rate variations cited above in collisional settings.

Geodetic strain rate estimates may be similar to strain rates inferred from the rock record of the last few million years of deformation. However, the geological records at several active zones of convergence show variation in the spatial distribution of strain rate on the multi-million year time scale. In the Himalayas, deformation can be interpreted to have gradually migrated onto the current locus at the orogenic front over a few tens of millions of years, as material accreted in the now $>$ 100 km wide zone of finite strain in the Himalayan arc (Fig. 2c)(Avouac, 2008). In the Central Andes, shortening currently accommodated by distributed strain in the foreland is faster than at 25 - 10 Ma, a time when convergence occurred at up to twice the current rate (Hindle et al., 2002). Hindle et al. (2002) interpreted this temporal change in strain rate partitioning to reflect a change in interseismic coupling, with convergence prior to 10 Ma dominantly accommodated by stable sliding localised along the megathrust, with little hanging wall shortening. This change from localised to distributed strain (and therefore strain rate) may reflect a change in the physical properties at the megathrust itself. Similarly, strain localised along many currently active faults in the Arabia-Eurasia collision zone occurs at strain rates that far exceed those calculated from their finite strain over the life time of the orogen (Allen et al., 2004). Allen et al. (2004) explain that currently active faults, located in areas of low elevation at the edges of the collision zone, initiated or took up increasing amounts of strain after 7 Ma. In earlier stages of collision, deformation occurred in what

is now uplifted regions with thickened crust. Similarly, shortening across the Himalayan mountain range does not occur on the high Tibetan Plateau, but has localised to the Main Himalayan Thrust Zone at the orogenic front in Nepal (Fig. 2c,d), for at least the last 20 Ma (Bilham et al., 1997; Bollinger et al., 2006; Avouac, 2008). These examples show that partitioning of deformation varies in time and space as convergent and collisional margins evolve, with deformation either slowing or accelerating in a given zone over time. Thus, a particular strain rate field is unlikely to be maintained for more than a few million years, substantially less than the lifetime of an orogen. Consequently, a bulk strain rate calculated from finite geological strain across an orogenic belt will not represent local, temporal strain rates that may control the bulk rheology at a given period of time.

4. Strain within and around faults

The earthquake cycle includes high strain rate slip that lasts from seconds to minutes, associated with brittle failure of the upper, elastic layer, followed by slower postseismic transient creep that decays towards steady-state interseismic deformation rates driven by viscous creep at depth (e.g. Hetland and Hager, 2005; Handy et al., 2007; Wang et al., 2012). Postseismic transients are attributed to viscoelastic relaxation of the lower crust and/or upper mantle, and/or afterslip caused by creep within the brittle fault zone (e.g. Wright et al., 2013). Variations in strain rates through the earthquake cycle are recorded as mutually crosscutting relationships between pseudotachylyte and mylonites in the rock record (Fig. 3a)(e.g. Sibson, 1980a; Price et al., 2012; Menegon et al., 2017), and maybe also by mutually cross-cutting con-

tinuous and discontinuous deformation structures (Fig. 3b)(Fagereng and Sibson, 2010; Rowe and Griffith, 2015). It is possible, maybe even likely, that peak strain rates derived from quartz paleopiezometry (e.g. Boutonnet et al., 2013; Viegas et al., 2016) could be related to post-seismic afterslip. In the following section, we review strain rates associated with the earthquake cycle on individual fault zones from both geodetic and geological perspectives, since both records agree that strain rate is not constant in time.

4.1. Surface deformation during the interseismic period

Geodetic observations record surface strain, and hence underestimate strain rates generated in the deep portions of fault zones. To illustrate, Savage and Burford (1973)'s widely used model of interseismic strain accumulation shows that surface velocity, u, at a distance x caused by slip rate of s on an infinitely long vertical, strike-slip fault with a locked elastic lid of thickness d is given by $u(x) = \frac{s}{\pi} \arctan \frac{x}{d}$. The shear strain rate is given by the derivative, such that $\dot{\gamma}(x) = \frac{s}{\pi d} \frac{1}{(1+x^2/d^2)}$, and the peak strain rate measured at the surface, $\dot{\gamma}_{max} = \frac{s}{\pi d}$, depends not only on the slip rate across the fault, but also the locking depth. Thus a slip rate of 1 cm/yr with a locking depth of 20 km would produce a peak surface strain rate of $5 \times 10^{-15} s^{-1}$, but $2 \times 10^{-14} s^{-1}$ for a locking depth of 5 km (Fig 4).

Thus surface strain rate alone is not a direct indicator of strain rates within a fault zone itself. Locking depth must also be considered when interpreting geodetic strain measurements. Locking depth is considered broadly equivalent to the frictional-viscous transition, and across the continents typically lies within a range of 14 ± 7 km (Wright et al., 2013). In contrast to oceanic crust, where locking depth varies smoothly as a function of temper-

ature, variations in continental locking depth do not correlate strongly with variations in crustal thickness, and it has therefore been suggested that variations in lithology and strain rate can be responsible (Wright et al., 2013). However, heat flow also varies significantly throughout continents, particularly as a function of tectonic regime, and long wavelength variations in thermal structure has successfully explained much of the depth variations in the seismologically determined locking depth (e.g. Sibson, 1984; Tse and Rice, 1986; McKenzie et al., 2005). Maggi et al. (2000) reviewed variations in earthquake focal depths, and suggested close correlation between elastic and seismogenic thickness, consistent with a first order dependence of locking depth on temperature, and secondary variations caused by lithology and fluid content.

Relatively few faults exhibit creeping behaviour, with slip extending all the way to the surface (Burford and Harsh, 1980; Lee et al., 2001; Harris, 2017). We expect the greatest rates of geodetic surface strain to be associated with these creeping faults. For example, the maximum rate of surface strain in California occurs on the creeping segment of the San Andreas fault, where slip rates up to 28 mm/yr generate surface strain rates that locally reach 2×10^{-13} s^{-1} (Tong et al., 2013)(Fig. 2a). Deformation associated with fluid flow within weakened fault rocks may well enhance shallow strain rate values, however, through alteration to frictionally weak minerals, or local elevation in fluid pressures (Rice, 1992; Wintsch et al., 1995). Ingleby and Wright (2017) have suggested that Omori-like decay of postseismic velocities is consistent with rate-and-state friction or power law shear zone models, implying that postseismic creep is also localised within a narrow tabular

zone. The fact that localised shear strain rate at depth is not fully recorded in the broad deformation field generated at the surface, may explain the order of magnitude difference between the Global Strain Rate Map (Kreemer et al., 2014), which considers the surface strain during interseismic periods, and the geological estimates of Pfiffner and Ramsay (1982), which consider the total intergrated strain.

4.2. Postseismic surface deformation

Elevated rates of surface deformation have been detected following more than 20 earthquake sequences (Wright et al., 2013). Models of the earthquake cycle show that viscous postseismic transients occur when the earthquake return period is much longer than the relaxation time (Savage and Prescott, 1978; Hetland and Hager, 2005). Models typically require Maxwell viscosities in the range $10^{17} - 7 \times 10^{19}$ Pas to fit observational strain data (Wright et al., 2013), but the associated changes in velocity are on the order of mm/yr and occur over wavelengths of tens of kilometers, so the associated surface strain rates rarely exceed 10^{-15} s^{-1} (e.g. Wang and Wright, 2012). As argued above, however, even slightly elevated surface strain rate could translate into a much greater increase in subsurface strain rate if it reflected postseismic strain localised along the deep extension of crustal faults.

Afterslip within the brittle fault zone can amount to a significant portion of the coseismic slip and produce surface displacements (e.g. Reilinger et al., 2000; Lee et al., 2006; D'Agostino et al., 2012). Afterslip is associated with velocity-strengthening frictional properties and attempts have been made to model it with rate-and-state friction (e.g. Perfettini and Avouac, 2007). However, high resolution GPS and InSAR studies show short wavelength (less

than a few km) variations in afterslip that can only be attributed to along-strike variations in frictional properties that possibly relate to differences in lithology (Barbot et al., 2009; Floyd et al., 2016). Because fault geometry and material properties at depth cannot be determined from observations of surface deformation patterns alone, we return to the geological data set to discuss strain accommodation within localised structures.

4.3. Shear Strain within Fault Zones

Geodetic models of strain accumulation cannot distinguish between slip on a single dislocation and that in a wider, tabular shear zone. Thus, estimates of strain rate within fault zones rely on geological observations of fault zone structure and dimensions. Sibson (2003) argued that the coseismic slip zone is commonly < 10 cm, so that the $\dot{\gamma}$ for seismic slip rates of 1 m/s becomes ≥ 10 s^{-1}, assuming the coseismic slip zone behaves as a continuum (Fig. 1a). Such localised principal slip zones, commonly embedded in wider damage zones, are typical of faults in crystalline rocks, as described by Chester and Logan (1987) for the Punchbowl fault, and also seen in several other continental faults (Fig. 3c). In contrast, Burford and Harsh (1980) reported that aseismic distortion along a creeping segment of the San Andreas fault is accommodated within simple shear zones up to 15 metres wide. In these zones, taking the creep rate as 10s of millimetres per year (e.g. Titus et al., 2006), $\dot{\gamma}$ can be approximated to an order of magnitude as 10^{-3} yr^{-1} or 10^{-11} s^{-1} (Fig. 1a), which is orders of magnitude faster than peak surface strain rates estimated at the resolution of the GSRM (Fig. 2a). While creeping faults in the upper crust are relatively unusual (Harris, 2017), mid- to lower crustal mylonites are typically inferred to accommodate steady creep,

or transient afterslip, over thicknesses of metres to kilometres. These shear zone widths imply strain rates ranging from 10^{-10} s^{-1} to 10^{-14} s^{-1} if slip rates are 1 - 10 mm/yr for shear zone width of 1 to 1000 m. Paleopiezometry results obtained from monomineralic quartz layers in viscous shear zones reflect strain rates in this range (Fig. 1a)(Gueydan et al., 2005; Boutonnet et al., 2013; Cross et al., 2015). Although some mylonites record relatively homogeneous strain (Fig. 3d), others have accumulated heterogeneous strain (Fig. 3e), implying variable degrees of localisation, which by our logic implies heterogeneous strain rate. An end-member example of such heterogeneity may be the discrete discontinuities observed within a zone of continuous deformation structures in mélange shear zones (Fagereng and Sibson, 2010; Ujiie et al., 2018)(Fig. 3f). In such mélanges, deformation occurs both in mm-cm wide principal slip zones, and distributed through matrix material over metres to hundreds of metres (Rowe et al., 2013). Thus, overall, localised deformation within high strain zones, which could be either steady or transient, appears to occur at rates that range from $< 10^{-10}$ s^{-1} to > 10 s^{-1}. Strain rates may be partitioned between individual, relatively homogeneous structures of different widths (Fig. 3c,d), or within a single, heterogeneous zone with variable degrees of strain localization (Fig. 3e,f).

We know that major shear zones typically contain thinner, anastomosing ultramylonites separating less deformed protomylonite to mylonite domains (e.g. Coward, 1990; Carreras, 2001; Rennie et al., 2013), meaning that strain rates within kilometre-scale shear zones are likely higher than the minimum estimated for their bulk. Evidence of strain localization, coupled with geometrical arguments of associated strain rate distribution over many orders

of magnitude (Fig. 1a), raise the question of how representative an average strain rate of 10^{-14} s^{-1} is in space. This point is emphasised by the range of strain rates inferred from calculations based on paleopiezometry (e.g. Gueydan et al., 2005)(Fig. 1a).

An additional set of field observations is how structures crosscut each other. Pseudotachylytes, 'fossilised' and variably crystallised friction melt interpreted as unequivocal evidence for earthquake slip (cf. Cowan, 1999), are reported both crosscutting and locally overprinted by mylonitic fabric in a range of tectonic settings (Sibson, 1980b; Price et al., 2012; White, 2012; Menegon et al., 2017)(Fig. 3a). This mutually crosscutting relationship implies a strain rate cycling between spatially distributed, but temporally steady or transient, viscous flow in the mylonite, likely at $\dot{\gamma} \leq 10^{-10}$ s^{-1}, and seismic slip at rates exceeding 10 s^{-1}. Examples of this strain rate cycling are particularly abundant in places where shear zones were active within relatively dry, strong, middle to lower crust (Sibson, 1980b; Menegon et al., 2017; Hawemann et al., 2018).

Recently, Rowe and Griffith (2015) noted evidence for several other indicators, in the rock record, of frictional heating to temperatures too low to produce melting, but which also imply dynamic, elevated strain rates. Similarly, other mutually crosscutting structures implying different degrees of strain localisation, such as hydrothermal veins and synmetamorphic foliations in subduction-related thrust-sense mélange shear zones (Fig. 3b), may also reflect cycling between relatively steady and dynamic strain rates (Fagereng et al., 2011, 2018; Ujiie et al., 2018). Such temporal variations are not captured by bulk strain rate estimates.

A note of caution on when and where to invoke strain localisation, however, is raised from observations of distributed strain in lower crustal and upper mantle rocks that lack signs of local high strain domains but record low differential stresses. For example, olivine grain size paleopiezometry in mantle xenoliths from the San Andreas transform fault system implies that increased mantle strain rates following crustal earthquakes can be accommodated by viscous dissipation of stress across a deforming zone much wider than in the overlying crust (Chatzaras et al., 2015). In another continental transform system, the Marlborough fault system of New Zealand's South Island, lack of Moho displacement and pervasive seismic anisotropy below the faulted upper crust has also been interpreted to show strain distributed over a wide zone in the lower crust and upper mantle (Wilson et al., 2004).

Handy et al. (2007) reviewed the structure of continental faults below the transition from dominantly frictional deformation in the upper crust to dominantly thermally activated viscous deformation in the lower crust and upper mantle. They make the point that the structure and rheology of faults and shear zones depends on their strain and thermal histories. Pennacchioni and Mancktelow (2018) make the case that geometry of small scale shear zones is pre-determined by precursor heterogeneities such as fractures or low viscosity compositional layers. However, over time, additional mechanisms to develop and grow weak zones in the lower crust include networking of shear zones with increasing strain (Handy, 1994) and reaction weakening with increasing fluid-rock interaction (Wintsch et al., 1995). Handy et al. (2007) raise examples of faults that show fast post-seismic deformation that is well fitted to a localised low viscosity zone in the lower crust, such as the

North Anatolian transform fault of Turkey (Bürgmann et al., 2002) and the Chelungpu thrust fault in Taiwan (Hsu et al., 2002), and contrast these with faults where only minor surface displacement is recorded after major earthquakes, including the 2001 Bhuj intraplate thrust event in India (Jade et al., 2002). In summary, it is likely that strain localisation in the lower crust requires some long-term thermal and/or kinematic weakening effects, although it is also promoted by stress increases down-dip of major earthquakes (Ellis and Stöckhert, 2004).

5. Spatiotemporal strain rate distribution and average strain rate

Overall, the observations we have collated show that where strain is not localised, strain rates are commonly 10^{-15} s^{-1} or slower, particularly if averaged over multiple earthquake cycles. Higher strain zones, in contrast. typically record strain rates of 10^{-14} s^{-1} or greater. Strain rates in high strain zones are likely underestimated, particularly where they are calculated from geodetic data. There are at least two reasons for this: (1) the spatial resolution of the data is not sufficient to identify high strain zones within anastomosing networks, which are known to exist from geological maps of shear zones (e.g. Carreras, 2001; Rennie et al., 2013); and (2) except along faults that creep steadily at the surface, surface strain rates underestimate strain rates on localised structures at depth (Fig. 4). We therefore highlight a need for care when comparing strain rates determined from geodetic data to those estimated from geological observations of rocks deformed at depth.

A picture arises of high strain zones accommodating strain rates faster than an average near 10^{-14} s^{-1}, separating lower strain blocks where transient

strain rate increases may occur, but average strain rate is less than 10^{-14} s^{-1}. Strain rate estimates based on a combination of microstructural observations and empirical stress-grain size and stress-strain rate relationships imply that the maximum strain rate within viscous high strain zones is in the range of 10^{-13} s^{-1} to 10^{-8} s^{-1} (e.g. Gueydan et al., 2005; Boutonnet et al., 2013; Viegas et al., 2016). Thus, while 10^{-14} s^{-1} may be a good estimate for the *time-averaged* bulk strain rate in an orogen, it does not represent the range of strain rates evidenced by the rock record. Low strain areas record slower strain rates. In contrast, localised high strain zones that are active for limited amounts of time accommodate strain rates higher than average (Fig. 1a).

On time scales comparable to the seismic cycle, seismological and geodetic networks in well instrumented, actively deforming areas record a spectrum of deformation rates (e.g. Peng and Gomberg, 2010). This spectrum ranges from plate tectonic displacement rates of mm/yr to earthquakes of m/s, through geodetically detected 'slow slip' of cm/week, to very low and low frequency earthquakes defined as seismic phenomena, with slip speeds slower than 1 m/s but sufficient to radiate seismic wave energy. Thus, in contrast to a paradigm where slip speeds are either steady or seismic, a range of values are allowed by the observations. This raises a question when interpreting strain rates that are elevated relative to a global average. Do they record steady viscous creep, transient slow slip, or post-seismic afterslip within a narrow zone or zones? This is a question to consider in future high resolution geophysical experiments, and highlights the point that strain rates are constant in neither space nor time.

In essence, any calculation of mid- to lower crustal rheology over multiple

earthquake cycles requires an estimate of strain rate. Pfiffner and Ramsay (1982)'s estimate of 10^{-14} s^{-1} is reasonable as a time averaged, bulk strain rate. However, strain rate is not steady in either time or space as the locus of deformation shifts in both time and space. The spatiotemporal variation in strain rate may, intriguingly, reflect changes in rheology with progressive strain. Another question with scope for additional future study is therefore what controls spatiotemporal variations in strain rate, particularly where geological and geodetic strain rates disagree, as in the India-Eurasia collision zones (Wang and Wright, 2012; Garthwaite et al., 2013) and the Andes (Hindle et al., 2002).

6. Conclusion and consequences

High strain zones that traverse the lithosphere, which accommodate the bulk of continental deformation at any one time, typically deform at local and transient rates exceeding both the 10^{-14} s^{-1} estimated from bulk geological reconstructions (Pfiffner and Ramsay, 1982), and absolute rates estimated from geodetically determined surface velocity fields (Kreemer et al., 2014). Two consequences of this conclusion are: (1) if higher strain rates are inserted in crustal strength curves, this implies either higher stresses or lower strengths within high strain zones, relative to predictions using a 10^{-14} s^{-1} strain rate; and (2) in cases of spatiotemporal strain rate variations on timescales of the earthquake cycle, there is a need for care in using time-averaged strain rates in estimating earthquake repeat times. The first of these consequences supports Bürgmann and Dresen (2008)'s banana split model for lithospheric strength distribution, with lateral strength and strain

gradients around weak, high strain, plate boundary zones.

Acknowledgements

Å.F. is funded by the European Research Council (ERC) under the European Union's Horizon 2020 research and innovation programme (starting grant agreement No 715836 "MICA"). J.B. is supported by COMET and NERC large grant 'Looking Inside the Continents from Space' (LICS) (grant code NE/K010913/1). We thank L. Goodwin and an anonymous reviewer for constructive and insightful reviews that significantly improved the manuscript.

References

Allen, M., Jackson, J., Walker, R., 2004. Late Cenozoic reorganization of the Arabia-Eurasia collision and the comparison of short-term and long-term deformation rates. Tectonics 23, TC2008, doi:10.1029/2003TC001530.

Avouac, J.-P., 2008. Dynamic processes in extensional and compressional settings-mountain building: from earthquakes to geological deformation. Treatise on Geophysics 6, 377–439.

Barbot, S., Fialko, Y., Bock, Y., 2009. Postseismic deformation due to the M_w 6.0 2004 Parkfield earthquake: Stress-driven creep on a fault with spatially variable rate-and-state friction parameters. Journal of Geophysical Research 114, B07405, doi:10.1029/2008JB005748.

Beaumont, C., Jamieson, R. A., Nguyen, M. H., Lee, B., 2001. Himalayan

681 tectonics explained by extrusion of a low-viscosity crustal channel coupled
682 to focused surface denudation. Nature 414, 738–742.

683 Behr, W. M., Platt, J. P., 2011. A naturally constrained stress profile through
684 the middle crust in an extensional terrane. Earth and Planetary Science
685 Letters 303, 181–192.

686 Bevis, M., 1988. Seismic slip and down-dip strain rates in Wadati-Benioff
687 zones. Science 240, 1317–1319.

688 Bilham, R., Larson, K., Freymueller, J., Jouanne, F., Le Fort, P., Leturmy,
689 P., Mugnier, J., Gamond, J., Glot, J., Martinod, J., Chaudury, N., Chi-
690 trakar, G., Gautam, U., Koirala, B., Pandey, M., Ranabhat, R., Sapkota,
691 S., Shrestha, P., Thakuri, M., Timilsina, U., Tiwari, D., Vidal, G., Vi-
692 gny, C., Galy, A., De Voogd, B., 1997. GPS measurements of present-day
693 convergence across the Nepal Himalaya. Nature 386 (6620), 61–64.

694 Bollinger, L., Henry, P., Avouac, J., 2006. Mountain building in the Nepal
695 Himalaya: Thermal and kinematic model. Earth and Planetary Science
696 Letters 244 (1), 58 – 71.

697 Boutonnet, E., Leloup, P. H., Sassier, C., Gardien, V., Ricard, Y., 2013.
698 Ductile strain rate measurements document long-term strain localization
699 in the continental crust. Geology 41, 819–822.

700 Burford, R. O., Harsh, P. W., 1980. Slip on the San Andreas fault in cen-
701 tral California from alignment array surveys. Bulletin of the Seismological
702 Society of America 70, 1233–1261.

Bürgmann, R., Dresen, G., 2008. Rheology of the lower crust and upper mantle: Evidence from rock mechanics, geodesy, and field observations. Annual Review of Earth and Planetary Sciences 36, 531–567.

Bürgmann, R., Ergintrav, P., Segall, P., Hearn, E. H., McClusky, S., Reilinger, R. E., Woith, H., Zschau, J., 2002. Time-dependent distributed afterslip on and deep below the Izmit earthquake rupture. Bulletin of the Seismological Society of America 92, 126–137.

Carreras, J., 2001. Zooming on Northern Cap de Creus shear zones. Journal of Structural Geology 23, 1457–1486.

Chatzaras, V., Tikoff, B., Newman, J., Withers, A. C., Drury, M. R., 2015. Mantle strength of the San Andreas fault system and the role of mantle-crust feedbacks. Geology 43, 891–894.

Chester, F. M., Logan, J. M., 1987. Composite planar fabric of gouge from the Punchbowl Fault, California. Journal of Structural Geology 9, 621–634.

Cowan, D. S., 1999. Do faults preserve a record of seismic slip? A field geologist's opinion. Journal of Structural Geology 21, 995–1001.

Coward, M. P., 1990. Shear zones at the Laxford front, NW Scotland and their significance in the interpretation of lower crustal structure. Journal of the Geological Society 147, 279–286.

Cross, A. J., Kidder, S., Prior, D. J., 2015. Using microstructures and TitaniQ thermobarometry of quartz sheared around garnet porphyroclasts to evaluate microstructural evolution and constrain an Alpine Fault Zone gotherm. Journal of Structural Geology 75, 17–31.

726 D'Agostino, N., Cheloni, D., Fornaro, G., Giuliani, R., Reale, D., 2012.
727 Space-time distribution of afterslip following the 2009 L'Aquila earthquake.
728 Journal of Geophysical Research: Solid Earth 117 (B2).

729 D'Agostino, N., England, P., Hunstad, I., Selvaggi, G., 2014. Gravitational
730 potential energy and active deformation in the Apennines. Earth and Plan-
731 etary Science Letters 397, 121–132.

732 Daout, S., Doin, M.-P., Peltzer, G., Lasserre, C., Socquet, A., Volat, M.,
733 Suhaus, H., 2018. Strain partitioning and present-day fault kinematics
734 in NW Tibet from Envisat SAR interferometry. Journal of Geophysical
735 Research 123, 2462–2483.

736 Ekström, G., England, P., 1989. Seismic strain rates in regions of dis-
737 tributed continental deformation. Journal of Geophysical Research 94,
738 10231–10257.

739 Elliott, J., Walters, R., Wright, T., 2016. The role of space-based observa-
740 tion in understanding and responding to active tectonics and earthquakes.
741 Nature communications 7, 13844.

742 Ellis, S., Stöckhert, B., 2004. Elevated stresses and creep rates beneath the
743 brittle-ductile transition caused by seismic faulting in the upper crust.
744 Journal of Geophysical Research 109, B05407, doi:10.1029/2003JB002744.

745 England, P., Houseman, G., Nocquet, J.-M., 2016. Constraints from GPS
746 measurements on the dynamics of deformation in Anatolia and the Aegean.
747 Journal of Geophysical Research: Solid Earth 121 (12), 8888–8916.

748 England, P., McKenzie, D., 1982. A thin viscous sheet model for continental
749 deformation. Geophysical Journal International 70 (2), 295–321.

750 England, P., Molnar, P., 1997. Active deformation of Asia: from kinematics
751 to dynamics. Science 278 (5338), 647–650.

752 England, P., Molnar, P., 2015. Rheology of the lithosphere beneath the cen-
753 tral and western Tien Shan. Journal of Geophysical Research: Solid Earth
754 120 (5), 3803–3823.

755 Fagereng, A., Diener, J. F. A., Meneghini, F., Harris, C., Kvadsheim, A.,
756 2018. Quartz vein formation by local dehydration embrittlement along the
757 deep, tremorgenic subduction thrust interface. Geology 46, 67–70.

758 Fagereng, A., Remitti, F., Sibson, R. H., 2011. Incrementally developed slick-
759 enfibers - geological record of repeating low stress-drop seismic events?
760 Tectonophysics 510, 381–386.

761 Fagereng, A., Sibson, R. H., 2010. Melange rheology and seismic style. Ge-
762 ology 38, 751–754, doi:10.1130/G30868.1.

763 Fialko, Y., 2006. Interseismic strain accumulation and the earthquake poten-
764 tial on the southern San Andreas fault system. Nature 441, 968–971.

765 Flesch, L. M., Haines, A. J., Holt, W. E., 2001. Dynamics of the India-Eurasia
766 collision zone. Journal of Geophysical Research: Solid Earth 106 (B8),
767 16435–16460.

768 Flesch, L. M., Holt, W. E., Haines, A. J., Shen-Tu, B., 2000. Dynamics of

the Pacific-North American plate boundary in the western United States. Science 287 (5454), 834–836.

Floyd, M. A., Walters, R. J., Elliott, J. R., Funning, G. J., Svarc, J. L., Murray, J. R., Hooper, A. J., Larsen, Y., Marinkovic, P., Bürgmann, R., et al., 2016. Spatial variations in fault friction related to lithology from rupture and afterslip of the 2014 South Napa, California, earthquake. Geophysical Research Letters 43 (13), 6808–6816.

Foster, D. A., Gray, D. R., 2007. Strain rate in Paleozoic thrust sheets, the western Lachlan Orogen, Australia: Strain analysis and fabric geochronology. In: Sears, J. W., Harms, T. A., Evenchick, C. A. (Eds.), Whence the Mountains? Inquiries into the Evolution of Orogenic Systems: A Volume in Honor of Raymond A. Price. Vol. 433 of Special Papers. Geological Society of America, pp. 349–368.

Freed, A. M., Bürgmann, R., 2004. Evidence for power-law flow in the Mojave desert mantle. Nature 430, 548–551.

Garthwaite, M. C., Wang, H., Wright, T. J., 2013. Broadscale interseismic deformation and fault slip rates in the central Tibetan Plateau observed using InSAR. Journal of Geophysical Research: Solid Earth 118 (9), 5071–5083.

Godin, L., Grujic, D., Law, R. D., Searle, M. P., 2006. Channel flow, ductile extrusion and exhumation in continental collision zones: an introduction. Geological Society of London Special Publications 268, 1–23.

Gourmelen, N., Amelung, F., 2005. Postseismic mantle relaxation in the Central Nevada Seismic Belt. Science 310, 1473–1476.

Gueydan, F., Mehl, C., Parra, T., 2005. Stress-strain rate history of a mid-crustal shear zone and the onset of brittle deformation inferred from quartz recrystallized grain size. In: Gapais, D., Brun, J. P., Cobbold, P. R. (Eds.), Deformation Mechanisms, Rheology and Tectonics: from Minerals to the Lithosphere. Vol. 243 of Special Publications. Geological Society of London, pp. 127–142.

Hacker, B. R., Yin, A., Christie, J. M., Davis, G. A., 1992. Stress magnitude, strain rate, and rheology of extended middle continental crust inferred from quartz grain sizes in the Whipple Mountains, California. Tectonics 11, 36–46.

Hacker, B. R., Yin, A., Christie, J. M., Snoke, A. W., 1990. Differential stress, strain rate, and temperatures of mylonitization in the Ruby Mountains, Nevada: Implications for the rate and duration of uplift. Journal of Geophysical Research 95, 8569–8580.

Haines, A., Holt, W., 1993. A procedure for obtaining the complete horizontal motions within zones of distributed deformation from the inversion of strain rate data. Journal of Geophysical Research: Solid Earth 98 (B7), 12057–12082.

Handy, M. R., 1994. The energetics of steady state heterogeneous shear in mylonitic rock. Materials Science and Engineering A174, 261–272.

Handy, M. R., Hirth, G., Bürgmann, R., 2007. Fault structure and rheology from the frictional-viscous transition downward. In: Handy, M. R., Hirth, G., Hovius, N. (Eds.), Tectonic Faults: Agents of Change on a Dynamic Earth. Vol. 95 of Dahlem Workshop Report. MIT Press, Cambridge, Mass., USA, pp. 139–181.

Harris, R. A., 2017. Large earthquakes and creeping faults. Reviews of Geophysics 55, 169–198.

Hawemann, F., Mancktelow, N. S., Wex, S., Camacho, A., Pennacchioni, G., 2018. Pseudotachylyte as field evidence for lower-crustal earthquakes during the intracontinental Petermann Orogeny (Musgrave Block, Central Australia). Solid Earth 9, 629–648.

Hearn, E., Johnson, K., Thatcher, W., 2010. Space Geodetic Data Improve Seismic Hazard Assessment in California: Workshop on Incorporating Geodetic Surface Deformation Data Into UCERF3; Pomona, California, 1–2 April 2010. Eos, Transactions American Geophysical Union 91 (38), 336–336.

Hetland, E., Hager, B., 2005. Postseismic and interseismic displacements near a strike-slip fault: A two-dimensional theory for general linear viscoelastic rheologies. Journal of Geophysical Research: Solid Earth 110 (B10).

Hicks, S. D., Shofnos, W., 1965. The determination of land emergence from sea level observations in southeast Alaska. Journal of Geophysical Research 70, 3315–3319.

Hindle, D., Kley, J., Stein, S., Dixon, T., Norabuena, E., 2002. consistency of geologic and geodetic displacements during andean orogenesis. Geophysical Research Letters 29, doi:10.1029/2001GL013757.

Hirth, G., Teyssier, C., Dunlap, W., 2001. An evaluation of quartzite flow laws based on comparisons between experimentally and naturally deformed rocks. International Journal of Earth Sciences 90, 77–87.

Holt, W. E., 1995. Flow fields within the Tonga slab determined from the moment tensors of deep earthquakes. Geophysical Research Letters 22, 989–992.

Holt, W. E., Haines, A. J., 1993. Velocity fields in deforming Asia from the inversion of earthquake-released strains. Tectonics 12, 1–20.

Hsu, Y.-J., Bechor, N., Segall, P., Yu, S.-B., Kuo, L.-C., Ma, K.-F., 2002. Rapid afterslip following the 1999 Chi-Chi Taiwan earthquake. Geophysical Research Letters 29, doi:10.1029/2002GL014967.

Huntington, K. W., Klepeis, K. A., with 66 community contributors, 2018. Challenges and opportunities for research in tectonics: Understanding deformation and the processes that link Earth systems, from geologic time to human time. A community vision document submitted to the U.S. National Science Foundation. Tech. rep., University of Washington.

Ingleby, T., Wright, T. J., 2017. Omori-like decay of postseismic velocities following continental earthquakes. Geophysical Research Letters 44, 3119–3130.

857 Jackson, J. A., McKenzie, D., 1988. The relationship between plate motions
858 and seismic moment tensors, and the rates of active deformation in the
859 Mediterranean and Middle East. Geophysical Journal of the Royal Astro-
860 nomical Society 93, 45–73.

861 Jade, S., Mukul, M., Parvez, I. A., Ananda, M. B., Kumar, P. D., Gaur,
862 V. K., 2002. Estimates of coseismic displacement and post-seismic defor-
863 mation using Global Positioning System geodesy for the Bhuj earthquake
864 of 26 January 2001. Current Science 82, 748–752.

865 Jamieson, R. A., Beaumont, C., Nguyen, M. H., Lee, B., 2002. Interaction of
866 metamorphism, deformation and exhumation in large convergent orogens.
867 Journal of Metamorphic Geology 20, 9–24.

868 Kaneko, Y., Fialko, Y., Sandwell, D. T., Tong, X., Furuya, M., 2013. In-
869 terseismic deformation and creep along the central section of the North
870 Anatolian Fault (Turkey): InSAR observations and implications for rate-
871 and-state friction properties. Journal of Geophysical Research 118, 316–
872 331.

873 Kostrov, V., 1974. Seismic moment and energy of earthquakes, and seismic
874 flow of rock. Izvestiya, Academy of Sciences, USSR, Physics of the solid
875 earth 1, 13–21.

876 Kreemer, C., Blewitt, G., Klein, E. C., 2014. A geodetic plate motion and
877 Global Strain Rate Model. Geochemistry Geophysics Geosystems 15, 3849–
878 3889.

879 Kreemer, C., Holt, W. E., Haines, A. J., 2002. The global moment rate
880 distribution within plate boundary zones. In: Stein, S., Freymueller, J. T.
881 (Eds.), Plate Boundary Zones. Vol. 30 of Geodynamics Series. American
882 Geophysical Union, Washington D.C., pp. 173–190.

883 Lee, J.-C., Angelier, J., Chu, H.-T., Hu, J.-C., Jeng, F.-S., 2001. Continuous
884 monitoring of an active fault in a plate suture zone: a creepmeter study of
885 the chihshang fault, eastern taiwan. Tectonophysics 333 (1), 219 – 240.

886 Lee, J.-C., Chu, H.-T., Angelier, J., Hu, J.-C., Chen, H.-Y., Yu, S.-B., 2006.
887 Quantitative analysis of surface coseismic faulting and postseismic creep
888 accompanying the 2003, Mw = 6.5, Chengkung earthquake in eastern Tai-
889 wan. Journal of Geophysical Research: Solid Earth 111 (B2).

890 Luan, F. C., Paterson, M. S., 1992. Preparation and deformation of synthetic
891 aggregates of quartz. Journal of Geophysical Research 97, 301–320.

892 Maggi, A., Jackson, J. A., McKenzie, D., Priestly, K., 2000. Earthquake
893 focal depths, effective elastic thickness, and the strength of continental
894 lithosphere. Geology 28, 495–498.

895 Masson, F., Chéry, J., Hatzfield, D., Martinod, J., Vernant, P., Tavakoli,
896 F., Ghafory-Ashtiani, M., 2005. Seismic versus aseismic deformation in
897 Iran inferred from earthquakes and geodetic data. Geophysical Journal
898 International 160, 217–226.

899 McCaffrey, R., 2005. Block kinematics of the Pacific–North America plate
900 boundary in the southwestern United States from inversion of GPS, seismo-

logical, and geologic data. Journal of Geophysical Research 110 (B07401, doi:10.1029/2004JB003307).

McKenzie, D., Jackson, J. A., Priestly, K., 2005. Thermal structure of oceanic and continental lithosphere. Earth and Planetary Science Letters 233, 337–349.

Menegon, L., Pennacchioni, G., Malaspina, N., Harris, K., Wood, E., 2017. Earthquakes as precursors of ductile shear zones in the dry and strong lower crust. Geochemistry, Geophysics, Geosystems 18 (12), 4356–4374.

Nicol, A., Mazengarb, C., Chanier, F., Rait, G., Uruski, C., Wallace, L., 2007. Tectonic evolution of the active Hikurangi subduction margin, New Zealand, since the Oligocene. Tectonics 26, TC4002, doi:10.1029/2006TC002090.

Nicol, A., Wallace, L., 2007. Temporal stability of deformation rates: Comparison of geological and geodetic observations, Hikurangi subduction margin, New Zealand. Earth and Planetary Science Letters 258, 397–413.

Norris, R. J., Cooper, A. F., 2003. Very high strains recorded in mylonites along the Alpine Fault, New Zealand: implications for the deep structure of plate boundary faults. Journal of Structural Geology 25, 2141–2157.

Peng, Z., Gomberg, J., 2010. An integrated perspective of the continuum between earthquakes and slow slip phenomena. Nature Geoscience 3, 599–607.

Pennacchioni, G., Mancktelow, N. S., 2018. Small-scale ductile shear zones:

Neither extending, nor thickening, nor narrowing. Earth-Science Reviews 184, 1–12.

Perfettini, H., Avouac, J.-P., 2007. Modeling afterslip and aftershocks following the 1992 Landers earthquake. Journal of Geophysical Research: Solid Earth 112 (B7).

Pfiffner, O. A., Ramsay, J. G., 1982. Constraints on geological strain rates: Arguments from finite strain states of naturally deformed rocks. Journal of Geophysical Research 87, 311–321.

Platt, J., 2015. Rheology of two-phase systems: a microphysical and observational approach. Journal of Structural Geology 77, 213–227.

Price, N. A., Johnson, S. E., Gerbi, C. C., West, D. P., 2012. Identifying deformed pseudotachylyte and its influence on the strength and evolution of a crustal shear zone at the base of the seismogenic zone. Tectonophysics 518-521, 63–83.

Reilinger, R. E., Ergintav, S., Bürgmann, R., McClusky, S., Lenk, O., Barka, A., Gurkan, O., Hearn, L., Feigl, K. L., Cakmak, R., Aktug, B., Ozener, H., Töksoz, M. N., 2000. Coseismic and Postseismic Fault Slip for the 17 August 1999, M = 7.5, Izmit, Turkey Earthquake. Science 289 (5484), 1519–1524.

Rennie, S. F., Fagereng, A., Diener, J. F. A., 2013. Strain distribution within a km-scale, mid-crustal shear zone: The Kuckaus Mylonite Zone, Namibia. Journal of Structural Geology 56, 57–69.

945 Rice, J. R., 1992. Fault stress states, pore pressure distributions, and the
946 weakness of the San Andreas fault. In: Evans, B., Wong, T. (Eds.), Fault
947 Mechanics and Transport Properties of Rocks. Academic Press, San Diego,
948 pp. 475–503.

949 Rowe, C. D., Griffith, W. A., 2015. Do faults preserve a record of seismic
950 slip? A second opinion. Journal of Structural Geology 78, 1–26.

951 Rowe, C. D., Moore, J., Remitti, F., IODP Expedition 343/343T Scientists,
952 2013. The thickness of subduction plate boundary faults from the seafloor
953 into the seismogenic zone. Geology 41, 991–994.

954 Royden, L. H., Burchfiel, B. C., King, R. W., Wang, E., Chen, Z., Shen, F.,
955 Liu, Y., 1997. Surface deformation and lower crustal flow in Eastern Tibet.
956 Science 276, 788–790.

957 Savage, J. C., Burford, R. O., 1973. Geodetic determination of relative plate
958 motion in central California. Journal of Geophysical Research 78, 832–845.

959 Savage, J. C., Prescott, W. H., 1978. Asthenosphere readjustment and the
960 earthquake cycle. Journal of Geophysical Research: Solid Earth 83 (B7),
961 3369–3376.

962 Shimizu, I., 2008. Theories and applicability of grain size piezometers, the
963 role of dynamic recrystallization mechanisms. Journal of Structural Geol-
964 ogy 30, 899–917.

965 Sibson, R. H., 1980a. Power dissipation and stress levels on faults in the
966 upper crust. Journal of Geophysical Research 85, 6239–6247.

967 Sibson, R. H., 1980b. Transient discontinuities in ductile shear zones. Journal
968 of Structural Geology 2, 165–171.

969 Sibson, R. H., 1984. Roughness at the base of the seismogenic zone: Con-
970 tributing factors. Journal of Geophysical Research 89, 5791–5799.

971 Sibson, R. H., 2003. Thickness of the seismic slip zone. Bulletin of the Seis-
972 mological Society of America 93, 1169–1178.

973 Stipp, M., Tullis, J., 2003. The recrystallized grain size piezometer for quartz.
974 Geophysical Research Letters 30, 2088, doi:10.1029/2003GL018444.

975 Suther, 1995. The Australia-Pacific boundary and Cenozoic plate motions in
976 the southwest Pacific: some constraints from Geosat data. Tectonics 14,
977 819–831.

978 Titus, S. J., DeMets, C., Tikoff, B., 2006. Thirty-Five-Year Creep Rates for
979 the Creeping Segment of the San Andreas Fault and the Effects of the 2004
980 Parkfield Earthquake: Constraints from Alignment Arrays, Continuous
981 Global Positioning System, and Creepmeters. Bulletin of the Seismological
982 Society of America 96, S250–S268.

983 Tong, X., Sandwell, D., Smith-Konter, B., 2013. High-resolution interseismic
984 velocity data along the San Andreas fault from GPS and InSAR. Journal
985 of Geophysical Research: Solid Earth 118 (1), 369–389.

986 Tse, S. T., Rice, J. R., 1986. Crustal earthquake instability in relation to
987 the depth variation of frictional slip properties. Journal of Geophysical
988 Research 91, 9452–9472.

989 Twiss, R. J., 1977. Theory and applicability of a recrystallized grain size
990 piezometer. Pure and Applied Geophysics 115, 227–244.

991 Ujiie, K., Saishu, H., Fagereng, A., Nishiyama, N., Otsubo, M., Masuyama,
992 H., Kagi, H., 2018. An explanation for episodic tremor and slow slip con-
993 strained by crack-seal veins and viscous shear in subduction mélange. Geo-
994 physical Research Letters 45, 5371–5379.

995 Viegas, G., Menegon, L., Archanjo, C., 2016. Brittle grain-size reduction of
996 feldspar, phase mixing and strain localization in granitoids at mid-crustal
997 conditions (Pernambuco shear zone, NE Brazil). Solid Earth 7, 375–396.

998 Wallace, L., Beavan, J., McCaffrey, R., Darby, D., 2004. Subduction zone
999 coupling and tectonic block rotations in the North Island, New Zealand.
1000 Journal of Geophysical Research 109, B12406, doi:10.1029/2004JB003241.

1001 Walters, R., England, P., Houseman, G., 2017. Constraints from GPS mea-
1002 surements on the dynamics of the zone of convergence between Arabia and
1003 Eurasia. Journal of Geophysical Research: Solid Earth 122 (2), 1470–1495.

1004 Wang, H., Wright, T., 2012. Satellite geodetic imaging reveals internal de-
1005 formation of western Tibet. Geophysical Research Letters 39 (7).

1006 Wang, K., Hu, Y., He, J., 2012. Deformation cycles of subduction earth-
1007 quakes in a viscoelastic Earth. Nature 484, 327–332.

1008 Wesnousky, S. G., 1994. The Gutenberg-Richter or characteristic earthquake
1009 distribution, which is it? Bulletin of the Seismological Society of America
1010 84, 1940–1959.

1011 Wessel, P., Smith, W. H. F., Scharroo, R., Luis, J. F., Wobbe, F., 2013.
1012 Generic Mapping Tools: Improved version released. Eos Trans. AGU 94,
1013 409–410.

1014 White, J. C., 2012. Paradoxical pseudotachylyte-fault melt outside the seis-
1015 mogenic zone. Journal of Structural Geology 38, 11–20.

1016 Whitten, C. A., 1956. Crustal movement in California and Nevada. Eos
1017 Trans. AGU 37, 393–398.

1018 Wilson, C. K., Jones, C. H., Molnar, P., Sheehan, A. F., Boyd, O. S., 2004.
1019 Distributed deformation in the lower crust and upper mantle beneath a
1020 continental strike-slip fault zone: Marlborough fault system, South Island,
1021 New Zealand. Geology 32, 837–840.

1022 Wintsch, R. P., Christoffersen, R., Kronenberg, A. K., 1995. Fluid-rock reac-
1023 tion weakening of fault zones. Journal of Geophysical Research-Solid Earth
1024 100 (B7), 13021–13032.

1025 Wright, T. J., Elliot, J. R., Wang, H., Ryder, I., 2013. Earthquake defor-
1026 mation and the Moho: Implications for the rheology of continental litho-
1027 sphere. Tectonophysics 609, 504–523.

Figure Captions

Figure 1: Examples of geologically estimated and geodetically calculated shear strain rates. a) Shear strain rate as a function of lengthscale, contoured for displacement rate in ideal simple shear. See text for details, and note that ellipses represent typical ranges but exceptions may occur. Note logarithmic axes, and that localisation of strain in zones thinner than one kilometre implies strain rates faster than 10^{-14} s^{-1} for displacement rates greater than 0.1 mm/yr, whereas estimates for deformation distributed over larger areas produces strain rates less than 10^{-15} s^{-1}. b) The distribution of strain rates taken from the deforming zones in the Global Strain Rate Model (Kreemer et al., 2014) compared to those of Pfiffner and Ramsay (1982). 'Deforming zones' are defined as plate boundaries and zones of diffuse deformation separating rigid plates, amounting to about 14 % of the Earth's surface (Kreemer et al., 2014).

Figure 2: Strain rate and seismicity in California, USA, and strain rate and topography for the Himalayan orogen. The strain rate maps show the 2nd invariant of strain rate as determined by the Global Strain Rate Map project (Kreemer et al., 2014) at 0.1° resolution. (a) Strain rate in California. Note the localisation, by at least an order of magnitude in strain rate, into the San Andreas fault system, which deforms at a strain rate greater than 10^{-14} s^{-1}. (b) Earthquakes with magnitude 3.0 or greater recorded in the NEIC catalogue since 1970. (c) Strain rate in the Himalayan orogen. Note the increase by at least an order of magnitude at the Himalayan front, as well as along a few other localised (and potentially transient) active structures. (d) Eleva-

tion from the GEBCO 2014 grid at 30 second resolution (The GEBCO_2014 Grid, version 20150318, www.gebco.net). Figures created in Generic Mapping Tools (Wessel et al., 2013).

Figure 3: Examples of strain heterogeneity in the rock record, as shown by brittle and ductile structures referring to mesoscopically discontinuous and continuous deformation. Kinematics indicated by yellow arrows. (a) Ductilely deformed pseudotachylyte (red arrow points to sheared injection vein) that also crosscuts metamorphic tectonite (blue arrow), Nusfjord, Norway (see Menegon et al., 2017, for more detail). (b) Hydrothermal veins crosscut metamorphic tectonite, but are also rotated and ductilely sheared. Both veins and rotated foliation record normal shear sense. A later brittle fault that is not ductilely deformed cuts through the centre of the veins implying further brittle localisation with time. Makimine mélange, Kyushu, Japan (Ujiie et al., 2018).(c) Localised brittle deformation in the core of the San Gabriel strike-slip fault, California, produced cataclasite in a narrow principal slip zone. (d) Strain localisation within a relatively homogeneous ductile shear zone, Nusfjord, Norway (see Menegon et al., 2017, for more detail). (e) Quartz and felspar porphyroclasts behaving as relatively rigid bodies within a lower viscosity biotite-rich matrix, Maud Belt, Antarctica. (f) A low competency matrix enveloping sheared competent clasts in the Chrystalls Beach Complex, New Zealand. Note thin cataclastic surfaces both parallel to, and cross-cutting, the matrix cleavage (examples in dashed yellow lines).

Figure 4: Simple model of surface velocity and strain rate caused by inter-

seismic slip on an infinitely long strike-slip fault (Savage and Burford, 1973). Both parameters are controlled by locking depth, meaning geodetic measurements of strain do not accurately record localised strain rates at depth, particularly for regions with deep brittle-ductile transitions.

Tables

Table 1: Estimates of viscosity and strain rate from thin viscous sheet models of various continental regions. The quoted viscosities assume a power law exponent of n=3.

Region	Viscosity Pas	Strain Rate s^{-1}	Reference
Arabian-Eurasia	$1 - 5 \times 10^{22}$	$3 \times 10^{-16} - 3 \times 10^{-15}$	Walters et al. (2017)
Anatolia	$3 \times 10^{21} - 10^{22}$	$6 \times 10^{-17} - 6 \times 10^{-15}$	England et al. (2016)
Tibet	10^{22}	$10^{-16} - 10^{-15}$	England and Molnar (1997)
Tibet	$5 \times 10^{21} - 5 \times 10^{22}$	$< 5 \times 10^{-15}$	Flesch et al. (2001)
Tien Shan	$1 - 4 \times 10^{22}$	10^{-15}	England and Molnar (2015)
North America	$10^{21} - 10^{22}$	-	Flesch et al. (2000)
Appenines	$1.5 - 3 \times 10^{21}$	2×10^{-15}	D'Agostino et al. (2014)

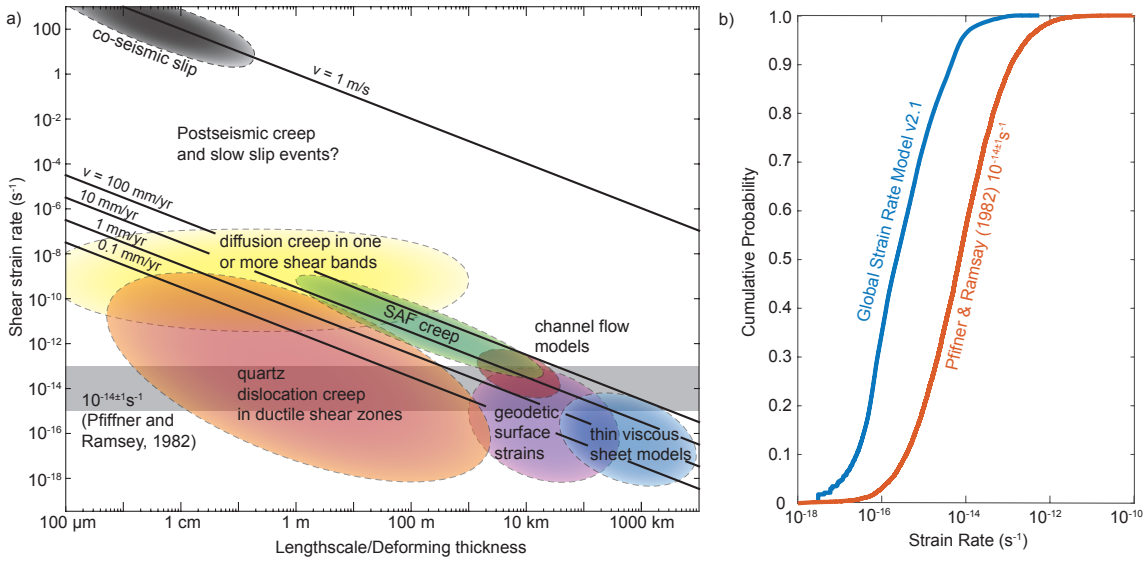
a)
co-seismic slip
v = 1 m/s
Postseismic creep
and slow slip events?
v = 100 mm/yr
10 mm/yr
1 mm/yr
0.1 mm/yr
diffusion creep in one
or more shear bands
SAF creep
channel flow
models
quartz
dislocation creep
in ductile shear zones
10^-14±1 s^-1
(Pfiffner and
Ramsey, 1982)
geodetic
surface
strains
thin viscous
sheet models
Shear strain rate (s^-1)
100 µm
1 cm
1 m
100 m
10 km
1000 km
Lengthscale/Deforming thickness
b)
Cumulative Probability
Global Strain Rate Model v2.1
Pfiffner & Ramsay (1982) 10^-14±1 s^-1
Strain Rate (s^-1)

Figure 1:

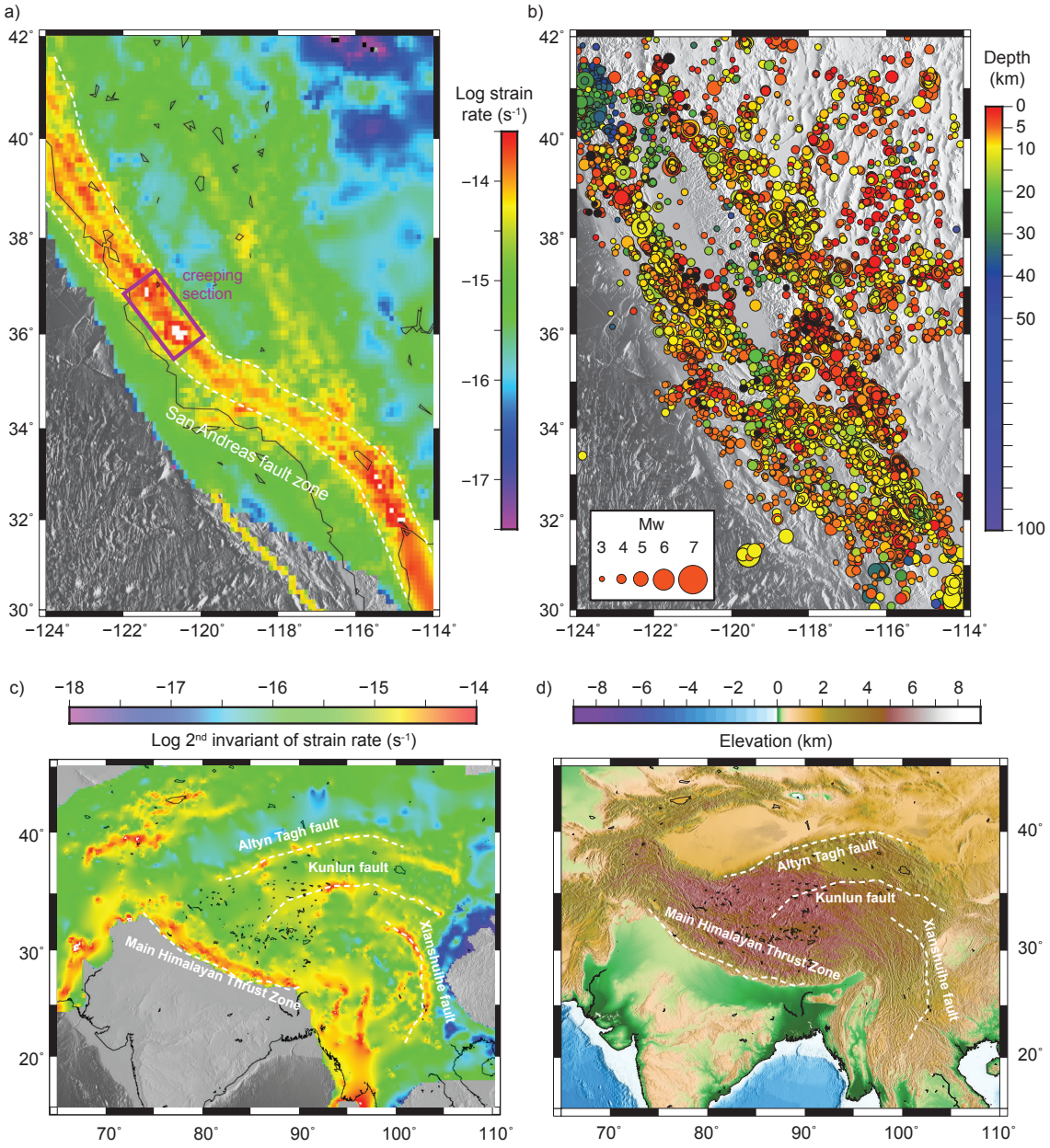
a)
b)
c)
d)
creeping section
San Andreas fault zone
Log strain rate (s-1)
Depth (km)
Mw
Log 2nd invariant of strain rate (s-1)
Elevation (km)
Altyn Tagh fault
Kunlun fault
Main Himalayan Thrust Zone
Xianshuihe fault

Figure 2:

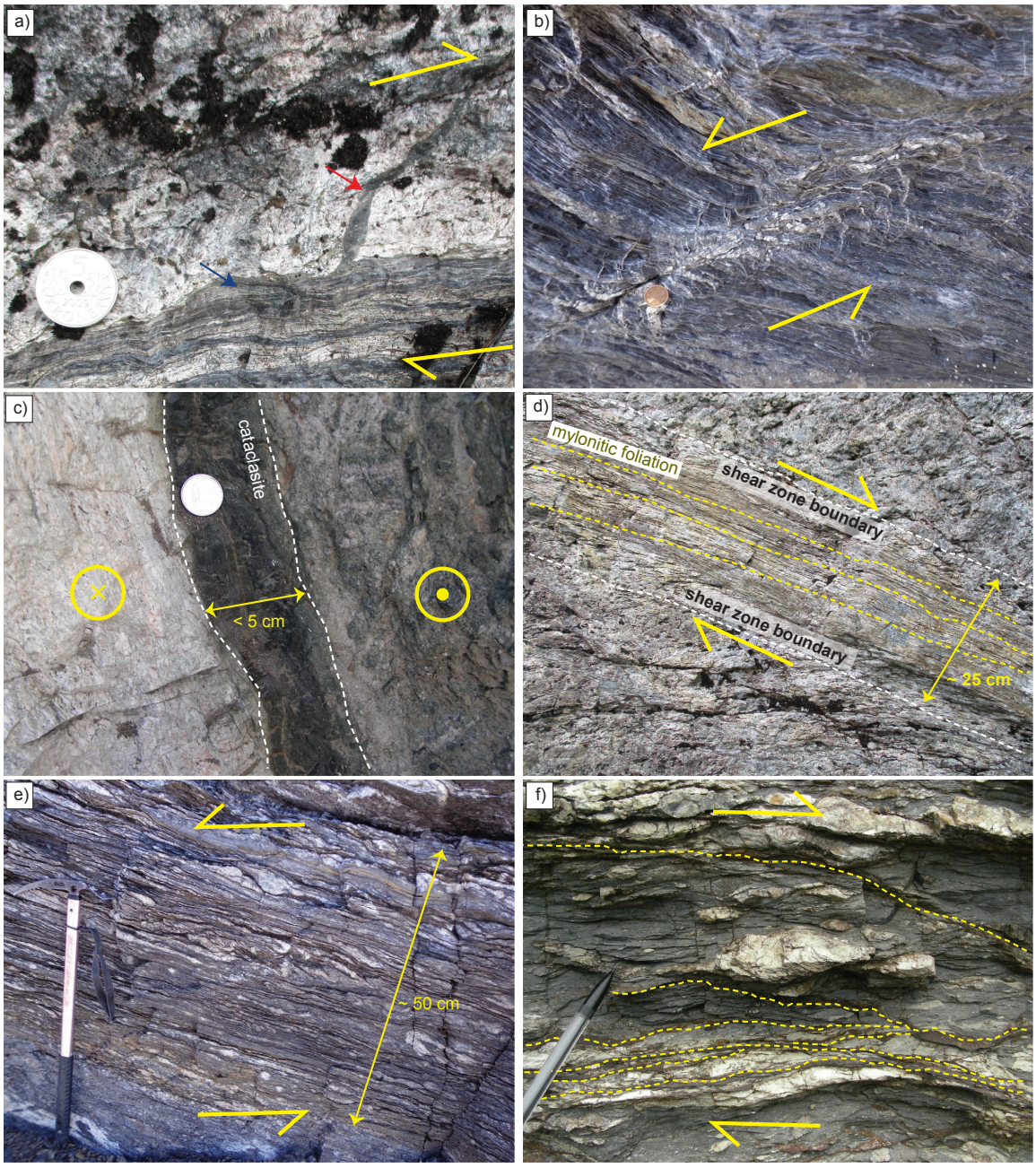
a)
b)
c)
cataclasite
< 5 cm
d)
mylonitic foliation
shear zone boundary
shear zone boundary
~ 25 cm
e)
~ 50 cm
f)

Figure 3:

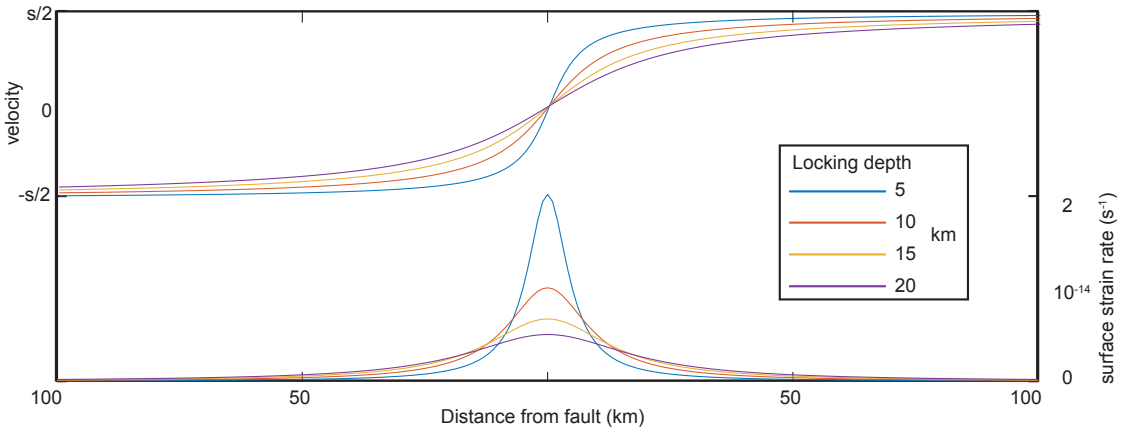
s/2
0
-s/2
velocity
Locking depth
5
10
15
20
km
2
10-14
0
surface strain rate (s-1)
100
50
50
100
Distance from fault (km)

Figure 4: